NASA/TM-2019-220338

THE INTERMEDIATE WAKE OF A THICK FLAT PLATE WITH A CIRCULAR TRAILING EDGE

Man Mohan Rai
Ames Research Center
Moffett Field, CA-94035

August 2019

NASA STI Program ... in Profile

Since its founding, NASA has been dedicated to the advancement of aeronautics and space science. The NASA scientific and technical information (STI) program plays a key part in helping NASA maintain this important role.

The NASA STI program operates under the auspices of the Agency Chief Information Officer. It collects, organizes, provides for archiving, and disseminates NASA's STI. The NASA STI program provides access to the NTRS Registered and its public interface, the NASA Technical Reports Server, thus providing one of the largest collections of aeronautical and space science STI in the world. Results are published in both non-NASA channels and by NASA in the NASA STI Report Series, which includes the following report types:

- TECHNICAL PUBLICATION. Reports of completed research or a major significant phase of research that present the results of NASA Programs and include extensive data or theoretical analysis. Includes compilations of significant scientific and technical data and information deemed to be of continuing reference value. NASA counterpart of peer-reviewed formal professional papers but has less stringent limitations on manuscript length and extent of graphic presentations.

- TECHNICAL MEMORANDUM. Scientific and technical findings that are preliminary or of specialized interest, e.g., quick release reports, working papers, and bibliographies that contain minimal annotation. Does not contain extensive analysis.

- CONTRACTOR REPORT. Scientific and technical findings by NASA-sponsored contractors and grantees.

- CONFERENCE PUBLICATION. Collected papers from scientific and technical conferences, symposia, seminars, or other meetings sponsored or co-sponsored by NASA.

- SPECIAL PUBLICATION. Scientific, technical, or historical information from NASA programs, projects, and missions, often concerned with subjects having substantial public interest.

- TECHNICAL TRANSLATION. English-language translations of foreign scientific and technical material pertinent to NASA's mission.

Specialized services also include organizing and publishing research results, distributing specialized research announcements and feeds, providing information desk and personal search support, and enabling data exchange services.

For more information about the NASA STI program, see the following:

- Access the NASA STI program home page at http://www.sti.nasa.gov

- E-mail your question to help@sti.nasa.gov

- Phone the NASA STI Information Desk at 757-864-9658

- Write to:
  NASA STI Information Desk
  Mail Stop 148
  NASA Langley Research Center
  Hampton, VA 23681-2199

NASA/TM-2019-220338

THE INTERMEDIATE WAKE OF A THICK FLAT PLATE WITH A CIRCULAR TRAILING EDGE

Man Mohan Rai
Ames Research Center
Moffett Field, California

National Aeronautics and
Space Administration

Ames Research Center
Moffett Field, California 94035-1000

August 2019

THE INTERMEDIATE WAKE OF A THICK FLAT PLATE WITH A CIRCULAR TRAILING EDGE

Man Mohan Rai*
NASA Ames Research Center, Moffett Field, CA-94035, USA

ABSTRACT

The intermediate wake region of a thick flat plate with a circular trailing edge (TE) is investigated with a direct numerical simulation (DNS). The upper and lower separating boundary layers are both turbulent and are statistically identical; the resulting wake is symmetric in the mean. Earlier research dealt with the near/very-near wake of the same plate (x/D < 13.0, x is the streamwise distance from the center of the circular TE and D is the plate-thickness/TE-diameter). In the present investigation the emphasis is on the evolution of shed-vortex structure and turbulence intensity distributions with increasing x; the focus is on the region 20.0 < x/D < 40.0. Profile similarity in wake velocity statistics is explored.

1. INTRODUCTION

An investigation of the wake of the thick flat plate with a circular trailing edge and turbulent separating boundary layers, was initiated by Rai (2013, 2014 & 2015). This was accomplished with the aid of direct numerical simulations (DNSs). The boundary layers as well as the wake were computed via DNS in these investigations. The separating boundary layers are fully turbulent well upstream of the trailing edge (TE) and are statistically identical in these investigations. The wake is symmetric in the mean and vortex shedding is vigorous in all the cases investigated (labelled Cases A - D). Unlike the case of the cylinder, the Reynolds number based on momentum thickness of the boundary layer just upstream of the TE (Re_θ) and the Reynolds number defined using the thickness of the flat plate or the diameter of its TE (Re_D), are independent parameters. Collectively, these articles address several aspects of the flat plate wake such as the instability of the detached shear layers (DSLs), entrainment, the distribution of phase-averaged turbulence intensities and shear stress and associated production terms. In Rai (2018a) shed vortex structure and phase-averaged velocity statistics in symmetric (turbulent boundary layers on both sides of the plate) and asymmetric (turbulent boundary layer on the plate upper surface and a laminar one on the lower surface) wakes are compared (identical thick-plate geometry, near wake, in both cases).

The investigations reported in Cantwell & Coles (1983), Hussain & Hayakawa (1987), Hayakawa & Hussain (1989) and Matsumura & Antonia (1993) are of importance to the present study. They are referred to hereafter as the investigations of **CC**, **HH1**, **HH2** and **MA**, respectively. In **CC** the turbulent near wake of a circular cylinder (Re_D = 140,000) is investigated with the aid of time- and phase-averaged velocity statistics. The authors make several inferences regarding the regions and mechanisms of turbulence production, the scales at which turbulence is produced, the importance of the pressure-strain term in redistributing turbulent kinetic energy, and the role of saddle points in entrainment and turbulence production.

In **HH1** the near and intermediate wake of a cylinder (Re_D = 13,000) is investigated. The authors note that the large-scale organized structures (for example, shed vortices) become increasingly irregular with increasing streamwise distance (x) from the TE. Irregularity is observed in streamwise spacing, cross-stream displacement (y), and the strength, size and shape of structures. In this experiment a linear cross-stream rake of eight **X**-wires is used to simultaneously measure velocities from which the instantaneous spanwise vorticity is then computed. An *optimal* list of procedures to capture the essential physics is

---

* Senior Researcher, Computational Sciences, Exploration Technology Directorate.

discussed and used in analyzing the measured data; identification of structures is based primarily on spanwise vorticity. Contour plots of smoothed spanwise vorticity in a (t, y) plane at x/D = 10, 20 & 40 clearly show increasing structure irregularity with increasing x (Figs 1a – 1g in **HH1**). Even at x/D = 10, both positive and negative shed vortices cross the wake centerline; however, the shape, size and strength of these vortices are fairly similar. At x/D = 20, for the most part, the negative vortices are above the wake centerline and the positive vortices are below this line. At x/D = 40 some negative vortices are observed almost entirely below the centerline, vortices of the same sign are adjacent to each other (without an intervening vortex of the opposite sign) and there is wide variation in the shape, size and strength of vortices. The observed flow features demonstrate the need for the elaborate set of rules of vortex identification developed in **HH1**. The authors observe that the growth in size of the shed vortices is not proportional to the spreading of the wake indicating that cross-stream wandering and three-dimensionality of these vortices increases with x. An extensive review of earlier work on coherent structures is provided in **HH1**.

The smoothed spanwise vorticity contours in Figs. 1a – 1g in **HH1** do not depict the true complexity in turbulent shed vortex structure. Figure 1 below, from Rai (2014, Fig. 6), shows contours of instantaneous spanwise vorticity in the very near wake at an instant when the lower shed vortex is being formed (flat plate case). It consists of smaller regions of vorticity of both signs, with regions of positive vorticity dominating. The regions of negative vorticity are largely from the upper shear layer. This complex vortex structure is retained as the shed vortex travels downstream. Figure 1 also shows the detached shear layer (DSL) instability in the upper DSL with the associated shear layer vortices (marked A and B). This complexity in vortex structure can be expected in the case of the cylinder wake (Re_D = 13,000) as well.

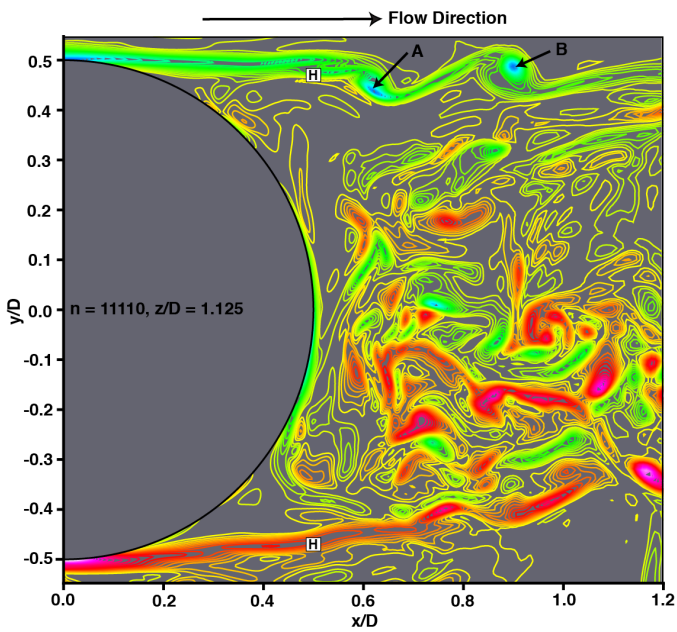

Fig. 1 Contours of instantaneous spanwise vorticity (flat plate wake, Case A, Rai 2014).

Some of the assertions of **HH1** with regard to the cylinder wake are: 1) intense production of turbulence by large scale coherent structures occurs mostly in the saddle region of the braid via vortex stretching, 2) turbulence produced in the braids is drained away from the saddle region and accumulated in the shed vortices, 3) this added turbulence counters decay and maintains turbulent energy in the shed vortices and 4) turbulence production involves the simultaneous generation of random fluctuations in all three velocity components. In Rai (2013) a DNS of the wake of a thick flat plate with vigorous vortex shedding provided phase-averaged production terms for streamwise and cross-stream turbulent normal intensity and shear stress. The results show that considerable production occurs in the braids, and that the rib vortices originating in the braids eventually wrap themselves around the vortex thus adding to the

turbulent energy in the vortex core. While this is consistent with the findings of **HH1**, the data of Rai (2013) also show *production* of streamwise intensity and *consumption* of cross-stream intensity in the core region. The underlying reasons are provided in Rai (2013). While the production of core-related streamwise intensity is consistent with the near-core peak in this component, the consumption of core-related cross-stream intensity is not consistent with the associated peak in this component that also occurs close to center of vortices. Since the phase-averaged turbulent transport term for this component is nearly zero at the centers of the cores it is most probably the velocity pressure gradient term that sustains the peak in the cross-stream component of intensity, that is, a redistribution of turbulent energy. The data of Rai (2013) also showed that the phase-averaged strain rate produces significantly less turbulent vorticity than that produced by turbulent stretching both in the braids and in the cores. Turbulent stretching was found to be particularly important in sustaining fluctuations in spanwise vorticity.

The three-dimensionality of organized structures in the intermediate wake of a cylinder (Re_D = 13,000) is investigated in **HH2**. Measurements of spanwise vorticity at x/D = 20 & 40 are provided. Two-point correlations in the spanwise direction (z) and spanwise vorticity are used to explore both the three-dimensionality of shed vortices and the increasing lack of their coherency with increasing x. Some of the principal observations of this study are as follows: 1) Two-point correlations in the z direction of smoothed spanwise vorticity decrease rapidly with increasing separation in the z-direction (especially at x/D = 40). Peak vorticity levels decrease considerably with increasing spanwise distance between the reference (x, y) plane (plane at which vortex core detection is performed) and the plane in question. This indicates considerable distortion of the shed vortices. The distortion could take many forms including bending and outright rupture of the shed vortex. 2) The data indicate the presence of rib vortices in the braids between successive shed vortices of opposite sign. The strength and size of these rib vortices may be similar to that of the shed vortices. 3) Any perturbation in vorticity in the braid region would tend to become aligned and organized in the direction of the principal strain and thus result in the generation of these rib vortices. The rib vortices are subject to stretching along the axis of the braid and in turn, distort the shed vortices.

Rib vortices were observed in the braids in Rai (2013) as well; many of them were paired (positive & negative) and some were solitary. Two-dimensional animations of vorticity showed the ribs in a braid wrapping themselves around the two shed vortices at the ends of the braid. The peak vorticity values within the ribs are significantly higher than the corresponding phase-averaged peak values (spanwise vorticity) in the cores of the neighboring shed vortices. Vorticity ratios as large as 9 were observed. Peak *instantaneous* spanwise vorticity levels in the cores, however, are much larger than the phase-averaged values. The cross-sectional shapes of the rib vortices were found to vary from elongated ellipses to nearly circular. The near-circular cross-sections were about 0.1D in 'diameter' whereas some of the elongated elliptical ones were as large as 0.35D in length. In comparison the shed vortices were about 1.0D in diameter at the x location of interest and thus much larger. The ribs weaken with increasing x. This is to be expected since the strain field in the braids becomes weaker with increasing x (the principal strain rates decreased by about 32% between the saddle points located just upstream of the positive vortex cores at x/D = 5.5 & 9.6). However, the peak vorticity values associated with the rib vortices continued to dominate the local phase-averaged peak spanwise vorticity in the shed vortices for x/D < 13.0.

To illustrate the structure of the vortex core, Fig. 2a (Fig. 11a from Rai 2013) provides instantaneous spanwise vorticity contours in an end-plane (y, z). This plane intersects a lower positive vortex when it is located at x/D = 5.7, at approximately its center. The fragmented nature of the core is evident. The level of fragmentation is expected since the vortices are formed by the roll-up of turbulent shear layers. The region y/D > 0.0 corresponds to the braid and not the shed vortex. The elongated positive vortices that comprise the core are evident (y/D < 0.0). Peak vorticity values are about 5 times as large as the peak phase-averaged value at x/D = 5.5. Interspersed among them are regions of *negative vorticity*. They are weaker and in general do not have the characteristic shape of the positive vortices. Some of the negative vorticity is accumulated in the initial formation of the positive shed vortices when they are in proximity to the turbulent shear layer on the opposing side. Figure 2b (Fig. 11b from Rai 2013) shows pressure contours in the same

plane and at the same time instant as in Fig. 11a. The nearly circular pressure minima above and below the core in Fig. 2b are rib vortices that have wrapped themselves around the core.

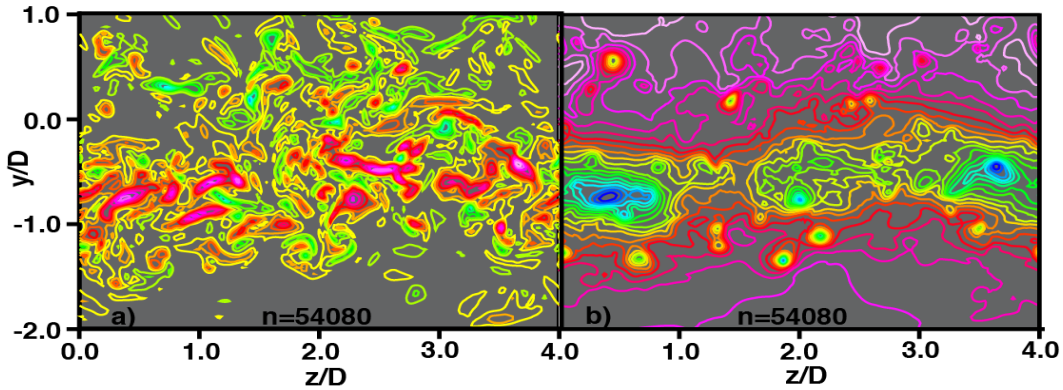

Fig. 2. Contours of a) spanwise vorticity; red/magenta represent high/highest positive values green/blue low/lowest negative values, yellow ≈ 0.0 and b) pressure in end plane (y, z) at x/D = 5.7 (Fig. 11, Rai 2013).

In **HH2** the three-dimensionality of the shed vortex is examined via two-point correlations of smoothed vorticity as well as phase-averaged spanwise vorticity contours at multiple spanwise locations (Figs. 7 & 8 in **HH2**). The degree of distortion reported in **HH2** was not evident in Rai (2013). However, the two flows are different (cylinder with laminar separating boundary layers and flat plate with turbulent separating boundary layers). More importantly, the largest value of x/D at which vortices were compared in Rai (2013) is 12.0, whereas in **HH2** the comparisons are further downstream (x/D = 20 & 40). Hence a greater loss of coherency in vortex structure can be expected in the data of **HH2**.

In **MA** the wake of a slightly heated cylinder (Re_D = 5830) is explored via hot-wire anemometry. Phase-averaged velocity and temperature statistics are provided in the region 10 < x/D < 40. The streamwise intensity profiles (periodic component) decrease rapidly with increasing x in relation to the total fluctuating value. The periodic profile is close to zero by x/D = 40; thus, the random component is the principal contributor to the total value. On the other hand, the corresponding cross-stream profiles show that the periodic component is the dominant contributor to the total value at x/D = 10 and makes a significant contribution to the total value even at x/D = 40. DNS data for this case is provided in Rai (2008). The computed normal intensity and shear stress profiles (total) are compared with the experimental data of **MA** at x/D = 10 & 40 and are found to be in good agreement. The computed ratio of the energies in the periodic and total signals (cross-stream component of velocity, v), along the centerline, are compared with experimental data from **MA** in Table 1. The DNS and experimental data are in fairly good agreement. The computational method used in the present investigation and in Rai (2008) are the same.

X/D	10.0	20.0	40.0
Matsumura & Antonia	85.3%	70.7%	49.0%
Rai (2008)	80.6%	65.0%	47.8%

Table 1. Comparison of computed and experimental ratio of energies in the periodic & total signals (centerline cross-stream component of velocity, Table 1 from Rai 2008 & 2013).

In the present investigation the emphasis is on the evolution of shed-vortex structure and turbulence intensity distributions with increasing x in the wake of a thick flat plate with turbulent separating boundary layers that are identical in the mean (symmetric wake). The focus is on the region 20.0 < x/D < 40.0. The data obtained in this region are compared with data in the near wake (x/D < 20) when appropriate. Potential profile similarity in velocity statistics is explored.

2. FLAT-PLATE COMPUTATIONAL GRID, FLOW/GEOMETRY PARAMETERS AND NUMERICAL METHOD

The computational region for the DNSs of the flat plates with a circular TE is divided into two zones to facilitate grid generation and provide adequate grid resolution for the wake. Figure 3 shows a typical plate cross-section and the two zones that comprise the computational region. The three-dimensional zones and grids are obtained by uniformly spacing copies of these two-dimensional zones in the z direction.

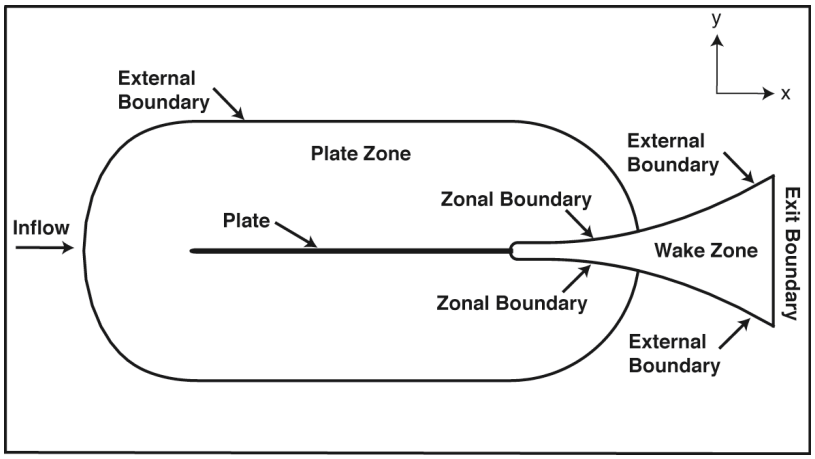

Figure 3. Midspan plate section and multiple zone discretization of the computational region for the circular TE cases (Rai 2013).

The plate zone is bounded by four boundaries; the plate surface (excluding the trailing edge), an external boundary and, two zonal boundaries (lower and upper) that interface with the wake zone. The wake zone is constructed to provide adequate grid resolution for the DSLs, the recirculation region and the wake. The boundaries of this zone include the circular TE, the upper and lower boundaries and the exit boundary. Both the upper and lower boundaries consist of a zonal boundary segment that interfaces with the plate zone and a second segment that serves as an external boundary. The coordinate system shown in Fig. 3 is only indicative of the coordinate directions; the origin is at the center of the circular TE (as in Fig. 4).

The placement of the various boundaries in relation to the plate surface in Case A is provided in Rai (2013). The vertical extent of the wake zone near the TE, where its upper/lower boundaries are horizontal is large enough to completely contain the wake in all cases (Fig. 4 in Rai 2013 clearly shows the adequacy of this dimension in Case A). The spanwise extent of the region in Case A is 4.0D.

Figure 4 shows representative grids in the vicinity of the TE in both zones. Both the grids have the same spacing in the wall normal direction at the plate surface. Downstream of the region of interest ($x/D \approx 13.5$ in Case A), the wake grid coarsens gradually in the x direction. This coarsening reduces computational costs and dissipates the wake to a degree that inviscid exit boundary conditions can be employed at the exit boundary of the wake zone. The wake grid for Case A (Rai 2014, 2015) was constructed with 741 grid points in the streamwise direction, 411 in the cross-stream direction and 256 in the spanwise direction (about 78 x 10^6 grid points). The resolution achieved along the centerline in the three spatial directions at $x/D = 10.0$ is approximately $\Delta x/\eta = 3.7$, $\Delta y/\eta = 2.2$ and $\Delta z/\eta = 2.1$ where η is the computed Kolmogorov length scale at the same location. The grid resolution in the plate grid in the x, y and z directions for this case is about 17.8, 0.84 and 6.6 wall units respectively, based on the wall shear velocity near the end of the plate. The adequacy of the grid resolution and domain size used is demonstrated in Rai (2013 & 2014).

In the present study the plate geometry is identical to Case A. Thus, Re_D (10,000) and Re_L (1.25 x 10^6, L is the plate length) are the same. Adequate grid resolution is provided until x/D is 43.75. The grid coarsens past this x location as in Case A. The present case will be referred to as Case AX (X stands for extended wake grid). The grid in the (x, y) plane in the near wake (x/D < 13.5) is identical in Cases A & AX The wake grid for Case AX was constructed with 1801 grid points in the streamwise direction, 411 in the cross-stream direction and 512 in the spanwise direction (about 379 x 10^6 grid points). The spanwise dimension is 8.0D.

The computations are performed at the same freestream Mach number as in Case A (0.2). Compressibility effects are quite small at this Mach number.

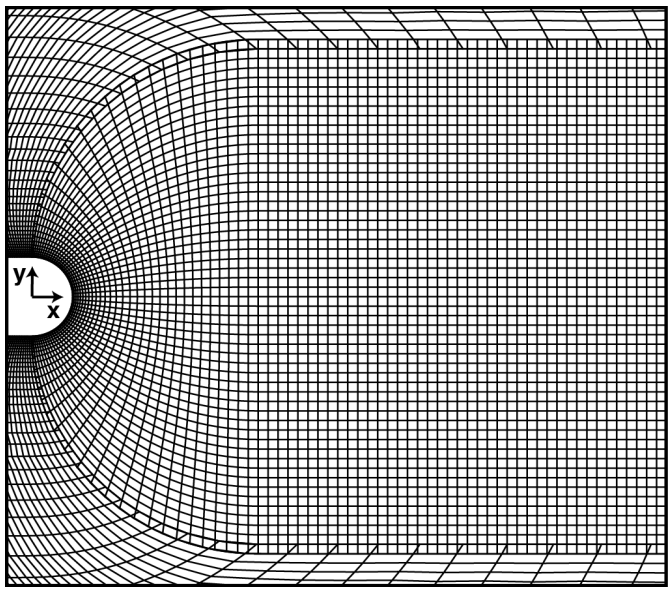

Figure 4. Representative grids in the plate and wake zones in the trailing edge region (Rai 2013).

A high-order accurate upwind-biased method is used here to compute the flow over the plate as well as that in the wake. The convective terms are computed using sixth- and seventh-order upwind-biased finite differences, both with seventh-order dissipation terms. These dissipation terms are the naturally occurring truncation error terms that are obtained in the upwind-biased finite-difference approximation to the convective terms. The viscous terms are computed with fourth-order central differences. The method is iterative-implicit in nature, multiple iterations are employed at each time-step to solve the nonlinear finite-difference equations arising from a fully implicit formulation; the method is second-order accurate in time.

The boundaries that contain the computational grids can be classified as natural and zonal boundaries in the circular TE cases. The natural boundaries include the external boundary of the plate grid, the surface of the plate, the exit boundary of the wake grid, the segments of the upper and lower boundaries of the wake grid labeled as “external boundary” in Fig. 3, and, the boundaries in the z direction. The upstream segment of the upper boundary between the plate and wake grids is an example of the zonal boundaries used in the computation. Periodic boundary conditions are imposed on the boundaries in the z direction (homogeneity in *z*) and no-slip/adiabatic wall conditions are used on the plate surface. Wall blowing/suction is implemented on a short segment on both the upper and lower surfaces of the plate to induce transition to turbulence. The boundary layer is turbulent well upstream of the trailing edge. The upper and lower transitional/turbulent boundary layers and the wake are all computed via DNS. The natural and zonal boundary conditions, and the high-order accurate upwind-biased finite-difference method used here are discussed in detail in the present author’s earlier articles cited in Rai (2015).

A discussion of the adequacy of the resolution used in the computations presented here via comparisons of DNS data obtained using the present method with 1) experimental cylinder wake data (Ong, Wallace & Moin, 1995) and 2) boundary layer data (Karlsson & Johansson, 1988) is provided in Rai (2017). An extensive comparison of the DNS data obtained for fully developed turbulent channel flow with an earlier version of the present method (lower-order of spatial accuracy for the inviscid terms, Rai & Moin 1991) and spectral method data (Kim, Moin & Moser, 1987) is also discussed in Rai (2017). These comparisons demonstrate the adequacy of the grid resolution used in the plate and wake grids. The adequacy of the size of the computational domain in all three spatial directions is also discussed at length in Rai (2017). In the interest of brevity these discussions have been omitted in the present article.

3. SHED-VORTEX STRUCTURE IN THE NEAR AND INTERMEDIATE WAKE

An interesting feature of the cylinder wake of **HH1** is that by x/D = 40.0 much of the repeating shed-vortex pattern of the near wake is lost; negative vortices are observed almost entirely below the centerline, vortices of the same sign are adjacent to each other (without an intervening vortex of the opposite sign) and there is significant variation in the shape, size and possibly the strength of vortices (Fig. 1 in **HH1**). In **HH2** we see evidence of the loss of spanwise coherency of the shed vortices; spanwise distortion could take many forms including bending and outright rupture of the shed vortex. We begin here by exploring differences in shed vortex structure in Case AX and the cylinder experiments of **HH1** & **HH2**. It is important to keep in mind that the wake generators, Reynolds numbers based on diameter, and the state of the boundary layer at separation are different in the two cases. Despite these differences it is a good starting point in the process of understanding some of the characteristics of the intermittent wake of the thick flat plate with turbulent separating boundary layers. Figures 5a – 5c show a top view of instantaneous constant-pressure surfaces at three instants in time (separation time between 5a/5b and 5b/5c is four shedding periods, np in the figures represents the number of shedding periods past the initial flow field).

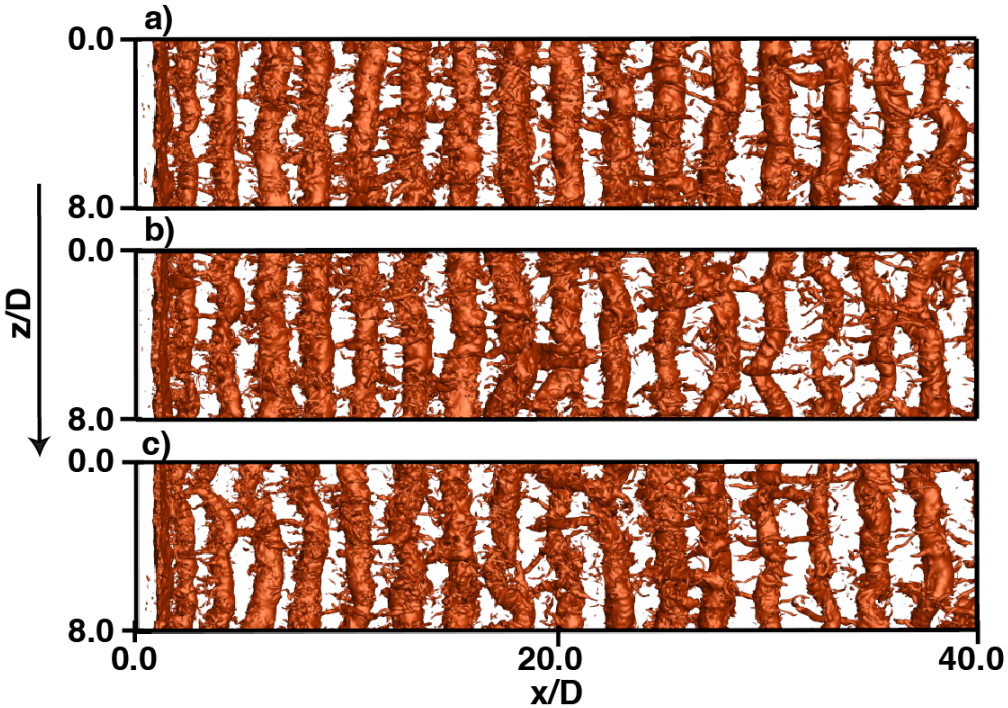

Figure 5. Instantaneous constant pressure surfaces showing shed-vortex structure in the wake at a) np = 16, b) np = 20, c) np = 24; top view.

Each approximately vertical column in Figs. 5a-5c corresponds to a shed vortex. Although some spanwise distortion is evident, for the most part, we have well defined shed vortices over the entire length (up to x/D = 40.0). Rupture of shed vortices is absent. Rib vortices spanning the braid regions between successive shed vortices are also observed. They seem to occur less frequently and seem to be weaker for x/D > 20.0. As mentioned earlier, this is to be expected since the strain field in the braid region gets weaker with increasing x (weaker shed vortices). This aspect will be addressed via phase-averaged intensity distributions later in this article. Figures 6a – 6c are corresponding side views of the pressure surfaces of Figs. 5a - 5c. All the positive shed vortices, even for x/D > 20.0, are almost entirely below the wake centerline (black horizontal line in the center of each sub-plot) and the negative vortices are above this line. The *across-centerline movement* (ACM) of the shed vortices observed in the **HH1** for x/D > 20.0 is absent here (described as *frequent excursions of structures across the centerline* at x/D = 40.0 in **HH1**). As in Figs. 5a-5c, rib vortices in the braids are observed in Figs. 6a-6c as well.

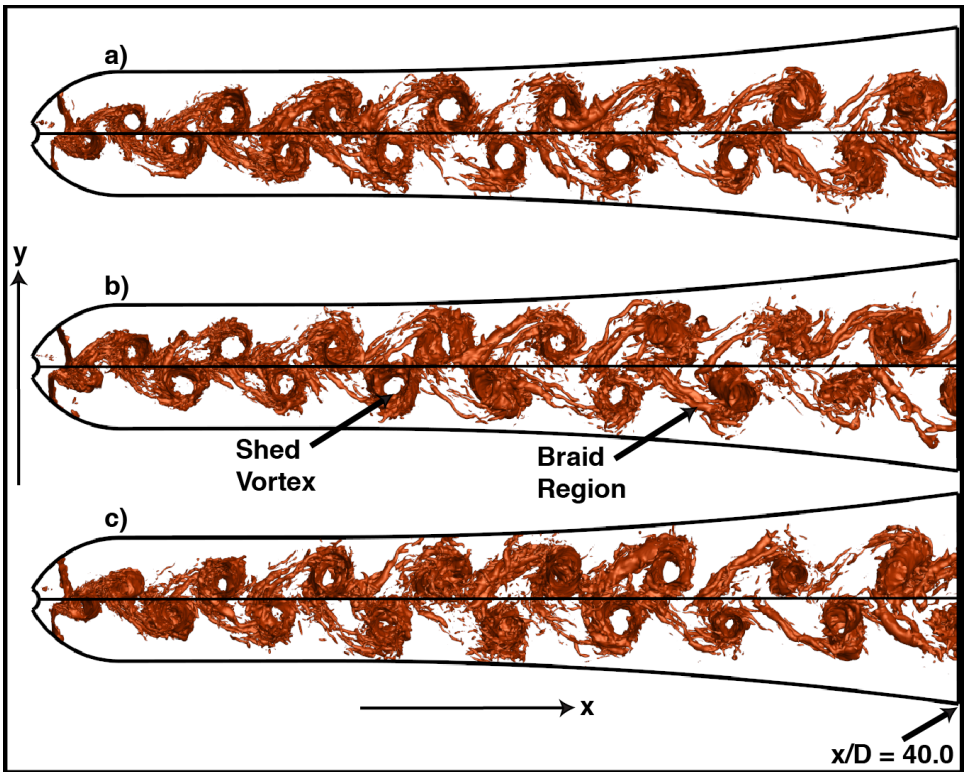

Figure 6. Instantaneous constant pressure surfaces showing shed-vortex structure in the wake at a) np = 16, b) np =20, c) np = 24; side view.

Figures 5a – 5c indicate that for fairly long periods of time there is relatively little spanwise distortion of the shed vortices and Figs. 6a - 6c do not indicate ACM of these vortices. However, the shed vortices in Case AX do exhibit rupture/distortion, albeit infrequently. Figures 7a – 7c show top views of instantaneous constant pressure surfaces at np = 32, 36 & 40, respectively. Figure 7a shows a region of rupture/distortion (20.0 < x/D < 26.0, see arrow). Figure 7b shows this region further downstream at a later time (see arrow). Figure 7c shows a relatively well-defined set of vortices and the restoration of the vortex street. Figures 8a-8c are corresponding side-views of Figs. 7a - 7c. Remarkably, even during the period of rupture, ACM of shed vortices is absent. ACM of a vortex should be visible in a side view because Fig. 8 shows *surfaces* of constant pressure and not pressure contours in an (x, y) plane. Contours of instantaneous pressure in an (x, y) plane at z/D = 2.0 (z location representative of the rupture) and np = 32 were also plotted. They show weak pressure minima in the region of rupture but not ACM of shed vortices (plot not included here).

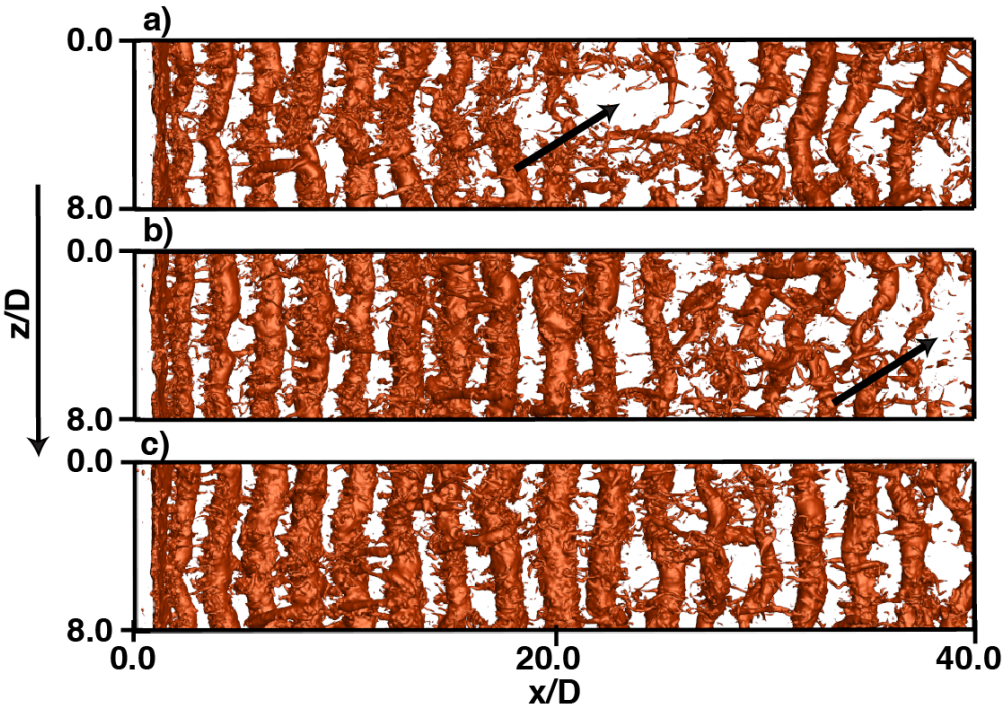

Figure 7. Instantaneous constant pressure surfaces showing shed-vortex structure in the wake at a) np = 32, b) np = 36, c) np = 40; top view.

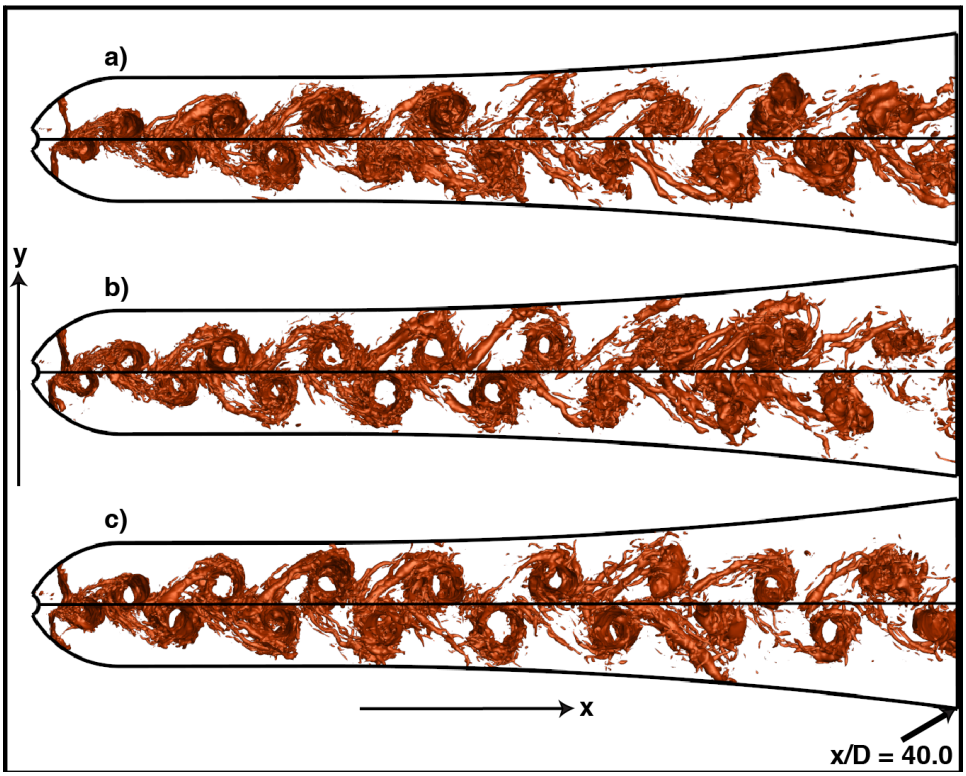

Figure 8. Instantaneous constant pressure surfaces showing shed-vortex structure in the wake at a) np = 32, b) np = 36, c) np = 40; side view.

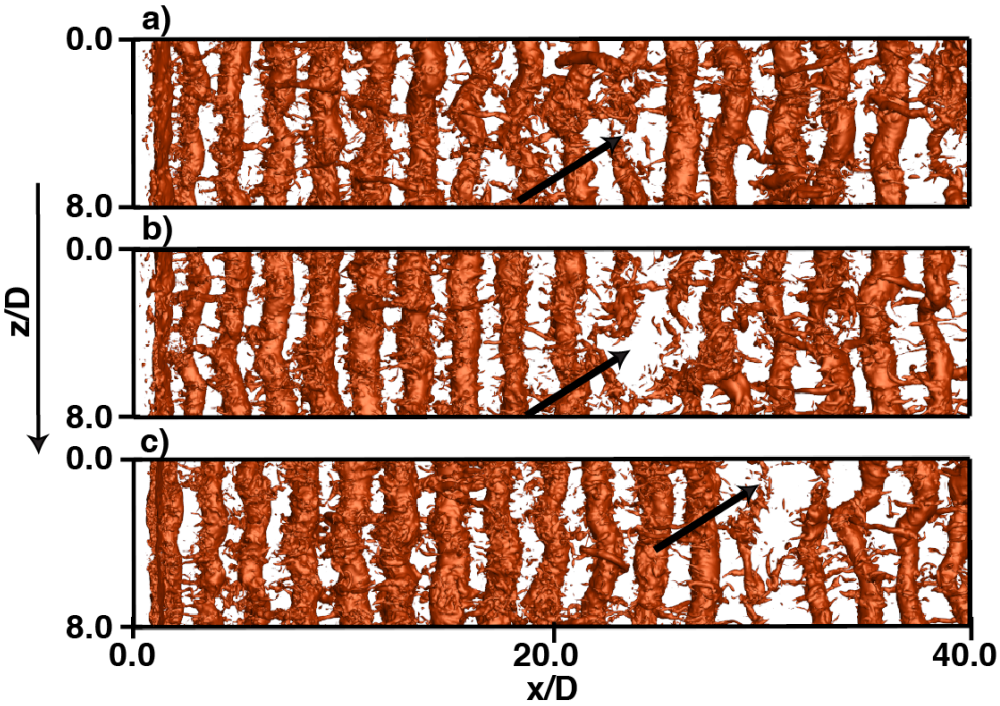

Figure 9. Instantaneous constant pressure surfaces showing shed-vortex structure in the wake at a) np = 0, b) np = 8, c) np = 52; top view.

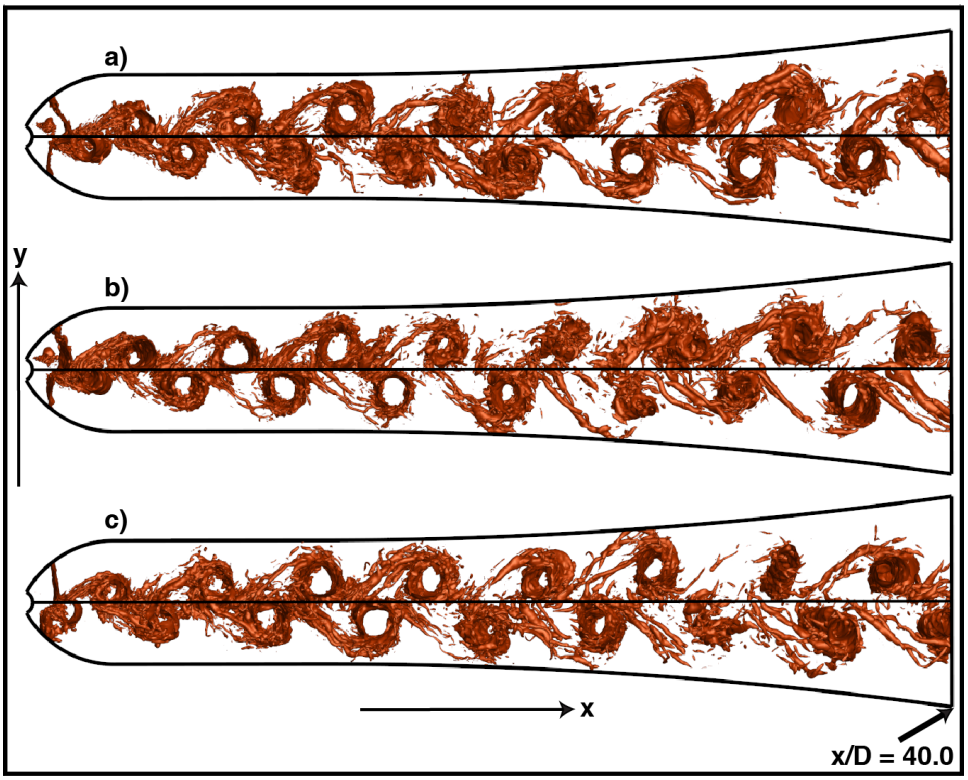

Figure 10. Instantaneous constant pressure surfaces showing shed-vortex structure in the wake at a) np = 0, b) np = 8, c) np = 52; side view.

Figures 9a – 9c show top views of instantaneous constant pressure surfaces at np = 0, 8 & 52, respectively. Unlike the sequence in Figs. 7a – 7c, the vortex disruptions (see arrows) are unrelated. Figures 10a – 10c are corresponding side-views of Figs. 9a - 9c. Clearly, in these instances as well there is no ACM of the shed vortex cores all the way up to x/D = 40.0. Of the several instants in time that were queried in this manner (both with and without vortex disruption/rupture) there were no instances with ACM of the shed vortex cores. Except for brief periods of rupture, Case AX shows a fairly well-ordered vortex street up to x/D = 40. This feature is in sharp contrast to that seen in the case of the cylinder (**HH1/HH2**).

Figure 11 shows centerline cross-stream velocity spectra obtained at x/D = 10.0 & 40.0 in Case AX. Frequencies are normalized with the shedding frequency and energies by the peak value obtained at x/D = 10.0. The two are very similar except for a small secondary peak obtained at x/D = 10.0 located at about three times the shedding frequency. As expected, the peak obtained at x/D = 40.0 is lower than that obtained at x/D = 10.0 because of the weakening of the shed vortices with increasing x and the corresponding decrease in the magnitude of fluctuating cross-stream velocity at the centerline. Occasional shed-vortex rupture/distortion seems to have little effect on centerline velocity spectra.

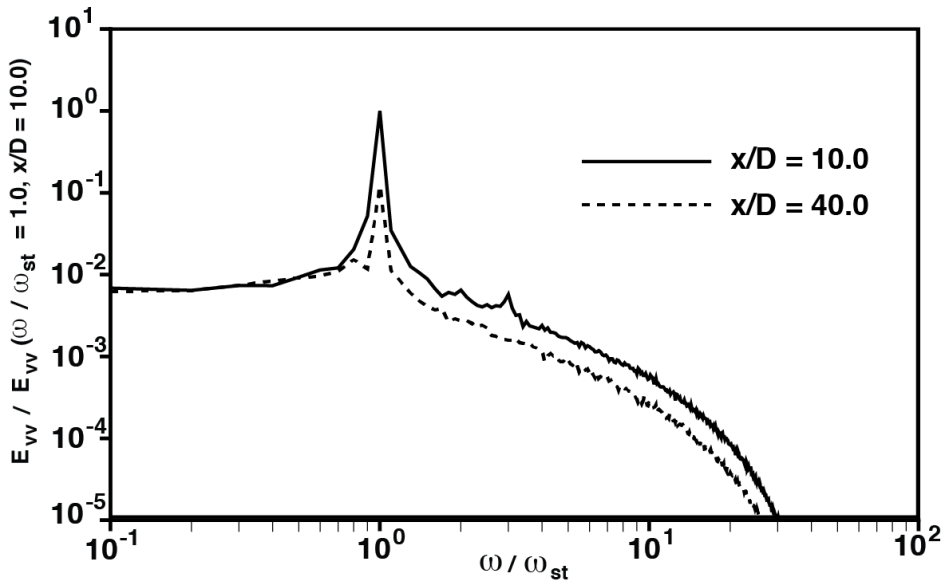

Figure 11. Centerline cross-stream velocity spectra obtained at x/D = 10.0 & 40.0.

In summary the vortex street in Case AX seems to be more stable than in the cylinder case of **HH1** and **HH2**, exhibiting shed vortex distortion infrequently and essentially no ACM of the cores of these vortices. An extensive discussion of possible modes of distortion of shed vortices in the case of the cylinder is provided in **HH2**.

4. VELOCITY STATISTICS IN THE INTERMEDIATE WAKE

Time-averaged distributions of intensity and shear stress (random and periodic fluctuating components and the combined or total value) in the *near wake* (Case A), are provided and discussed in Rai (2011). In this section we look at the time-averaged distribution of velocity statistics in the intermediate wake, in particular the onset of self-similarity in profiles of velocity and turbulence intensity. The fluctuating density, pressure and velocity components in the flow field are assumed to consist of a mean component, a periodic component at the shedding frequency ω_{st} (and harmonics thereof), and the random turbulent component as in Reynolds & Hussain (1972).

Thus, a flow variable q is written as

$$q = \overline{q} + q' + q'' \tag{1}$$

In Eq. 1 $\overline{q}$ is the mean value. The variables q' and q'' are the random and periodic fluctuating components, respectively. The phase-averaged value $< q >$ (average at constant phase) is given by

$$<q(\phi)> = \overline{q} + q''(\phi) \tag{2}$$

where ϕ is the phase, $0.0 \leq \phi \leq 1.0$. The computed data presented here were averaged in the z direction as well to obtain both the time-averages and phase-averages since the flow is homogeneous in this direction. The phase-averaging method used here is described in Rai (2013).

Figure 12 shows the distribution of time-averaged streamwise intensity (total) in the near/very-near wake. High intensity levels are evident in the separating boundary layers (arrow A), in the two off-center global maxima at x/D = 1.22 (arrow B) and also in the off-center layers further downstream (arrow C). The last two features are associated with the shed vortices. Figure 13 shows the distribution of streamwise intensity (total) both in the near and intermediate wake. Much of the complexity seen in the near wake is absent in the intermediate wake; the main feature of the downstream portion of the wake is the off-center peaks in profiles with a local minimum at the wake centerline. Distributions of the time-averaged streamwise velocity, cross-stream intensity and turbulent shear stress also show the same simplification in the intermediate wake (for the sake of brevity they are not included here). The simple distribution obtained downstream of x/D = 20.0 indicates the potential for self-similar streamwise intensity profiles in this region.

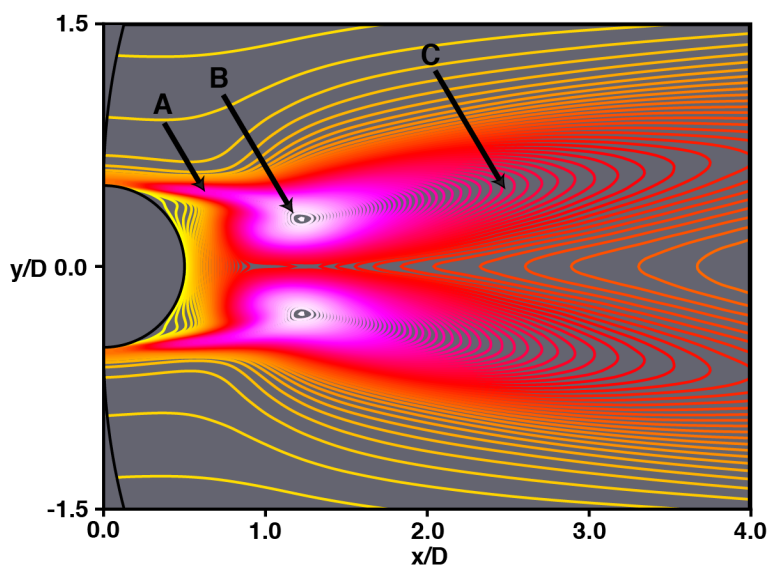

Figure 12. Contours of time-averaged streamwise intensity in the near wake.

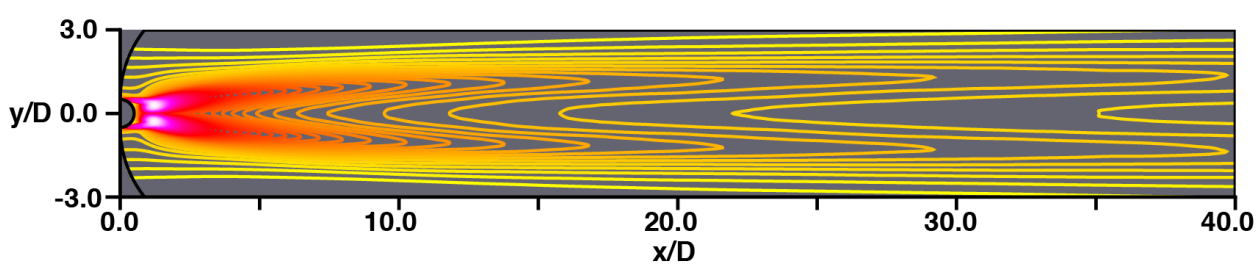

Figure 13. Contours of time-averaged streamwise intensity in the near and intermediate wake.

Much of the past work in establishing profile similarity of velocity statistics has dealt with the far wake where the maximum velocity defect is small compared to the freestream velocity. The more recent research that is presented in Hah & Lakshminarayana (1982) and Thomas & Liu (2004) deals with similarity in the near and intermediate wake. The wakes in both these studies exhibit little or no vortex shedding.

Experimentally obtained asymmetric airfoil wake data are provided in Hah & Lakshminarayana (1982). Asymmetry was achieved via three positive incidence angles. The suction side exhibits a thicker boundary layer than the pressure side. Data in the near and intermediate regions of the wake including cross-stream profiles of velocity, turbulence intensities and Reynolds shear stress are analyzed. When normalized with the defect velocity and wake half-thickness values, the velocity profiles exhibited similarity and also proximity to a Gaussian distribution except in the very near wake particularly in the outer wake region. Turbulent normal intensity profiles were found to become fairly symmetric at 1.5 chords from the trailing edge. When normalized by the *local maximum intensity*, and length scales corresponding to the half width of the *intensity profiles*, these profiles also collapsed reasonably well. However, deviations from a Gaussian distribution were observed in the very near wake and in the outer region of the wake.

An experimental investigation of symmetric and asymmetric turbulent wakes behind a flat plate is discussed in Thomas & Liu (2004). The thickness of the plate is tapered down to 1.6 mm at a taper angle of 2.2^{o} in the last 0.2 meters of the plate length. Velocity defect profiles for the symmetric case showed excellent similarity while the asymmetric profiles collapsed reasonably well although not quite symmetric about the centerline. The cross-stream distance in the asymmetric case was measured from the location at which maximum velocity defect occurred, and it was normalized by the respective wake thickness (upper and lower). Both cases showed a fairly good collapse of profiles of the ratio of the Reynolds shear stress and turbulent kinetic energy.

George (1989) provides an overview of the important concepts of self-similarity in turbulent flows, particularly wakes and jets. One possible classification of self-similar flows, into fully self-preserving, partially self-preserving and locally self-preserving (scaling with local quantities, governing equations not allowing self-preserving solutions) is presented here. Self-preservation at different levels, such as mean quantities, second-order moments etc., and, the conditions required to be satisfied for self-similarity in a given flow are discussed. A discussion of the impact of initial conditions on self-similarity in a given flow and across similar flows, such as the far wake of different wake generators is also provided.

The possibility of obtaining self-similarity in the near wake in Case A was explored in Rai (2011). The conventional approach to obtaining self-similarity using a single length and velocity scale yielded a marginal collapse of velocity and intensity profiles. An investigation of both the phase-averaged distributions of streamwise and cross-stream intensity profiles indicated the presence of more than one velocity and length scale in the near wake. A method to incorporate multiple length scales and “natural origins” that uses nonlinear transforms and a sub-division of the region of interest in the cross-stream direction was proposed. An excellent collapse of the velocity and intensity profiles in the entire near wake is obtained using this method. The study indicated that a more generalized version of self-similarity, present in some flows, may not be discernible with the use of a single velocity and length scale. Multiple velocity and length scales that may be present need to be accounted for to determine the presence of such self-similarity.

In the present investigation we explore the possibility of obtaining a collapse of profiles using a conventional linear transform (single length scale) and a single velocity scale (one set per variable) in the *intermediate wake*. Figure 14 shows velocity defect profiles at x/D = 20.0, 30.0 & 40.0. The wake half-width (δ_1) is used to normalize *y*. All three profiles collapse well with the ones at x/D = 30.0 & 40.0 being nearly indistinguishable. Figure 15 shows streamwise intensity profiles at x/D = 5.5, 20.0, 30.0, 40.0. The peak value is used to normalize intensity values and *y* is normalized using δ_2, the distance from the centerline to the peak. Figure 15 clearly shows a good collapse of profiles at x/D = 20.0, 30.0 and 40.0. The profile

obtained at x/D = 5.5 (near wake) does not follow this trend; it has been included to aid in the discussion of the presence of multiple length and velocity scales in the near wake which prevent profile collapse in this region with the very simple normalization used here.

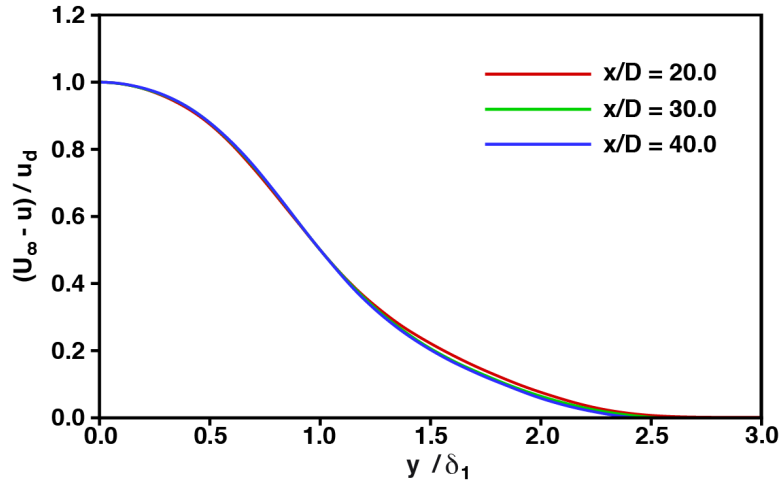

Figure 14. Velocity defect profiles at x/D = 20.0, 30.0 & 40.0.

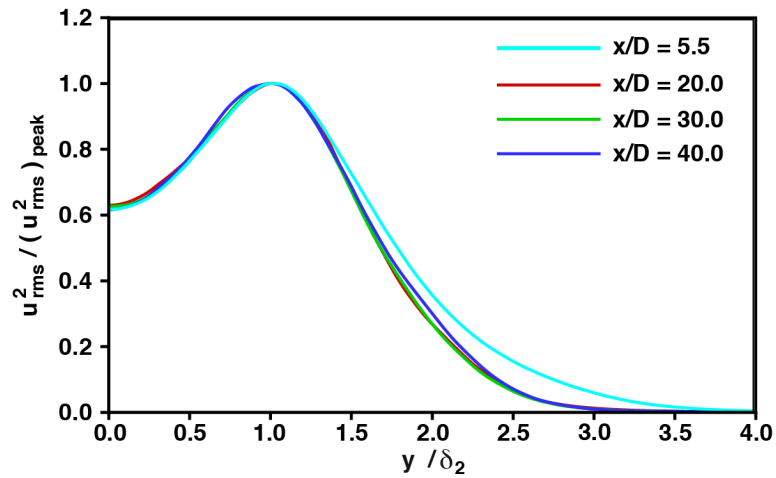

Figure 15. Streamwise intensity (total) profiles at x/D = 5.5, 20.0, 30.0 & 40.0.

Figure 16 shows cross-stream intensity profiles at x/D = 20.0, 30.0, 40.0. As in Fig. 15 the peak value is used to normalize intensity values and *y* is normalized using δ_3 the distance from the centerline to the peak. While the profiles at x/D = 30.0 & 40.0 collapse very well, the one at x/D = 20.0 does not. Cross-stream velocity profiles seem to take longer to exhibit self-similarity than streamwise intensity profiles. It is surprising that the velocity and intensity profiles collapse as well they do in the intermediate wake given that the shed vortices continue to be relatively powerful in this region (ratio of peak phase-averaged vorticity when the vortex cores are located at x/D = 40.0 & 5.5 is about 0.49). In the following we explore contributors to the observed self-similarity.

Figures 17a & 17b show contours of phase-averaged streamwise intensity (random component only) when the *upper* shed vortex is at x/D = 5.5 & 40.0, respectively; or, stated more simply, when x_{usvl}/D = 5.5 & 40.0 where the subscript '*usvl'* stands for 'upper shed vortex location'. The vertical white line on the left in the two sub-plots is at the same x/D as the upper shed vortex (referred to as location V in the following figures, irrespective of shed vortex location). The line on the right is approximately halfway between the

upper shed vortex of interest and the lower shed vortex immediately downstream; it intersects the braid region (referred to as location M henceforth). The minimum and maximum values and number of contours used in Figs. 17a & 17b are the same and so they can be directly compared.

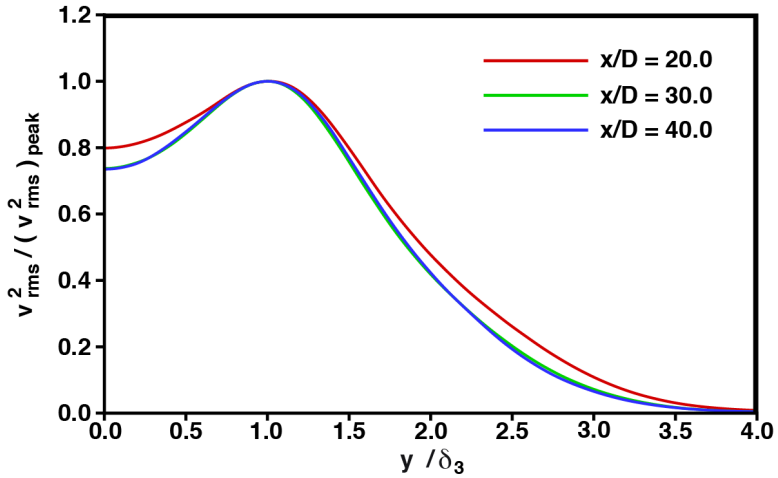

Figure 16. Cross-stream intensity (total) profiles at x/D = 20.0, 30.0 & 40.0.

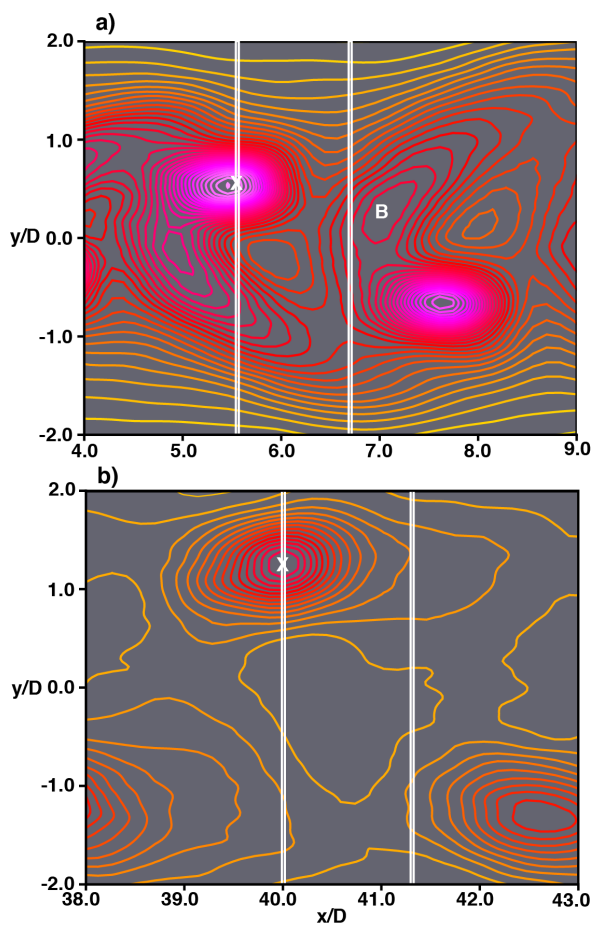

Figure 17. Contours of phase-averaged streamwise intensity (random component) when the upper shed vortex is located at a) x/D = 5.5 & b) x/D = 40.0.

Figure 17a shows a peak in intensity very near the shed vortex cores (upper shed vortex marked with an X). In addition, there is a peak in the braid region (marked with a "B"). Rib vortices in this portion of the braid are essentially vertical and thus contribute significantly to random fluctuations in streamwise velocity resulting in the braid related peak in streamwise intensity. In contrast, at x_{usvl}/D = 40.0 (Fig. 17b), while the core-related intensity levels continue to be significant (ratio of peak values at x_{usvl}/D = 40.0 & 5.5 is 0.54), braid related intensities levels are considerably weaker than in Fig. 17a. This is not surprising because braid related strain rates decrease with increasing x and thus the rib vortices tend to be fewer and weaker. As noted in Rai (2013), in Case A, the principal strain rates decrease by about 32% between the saddle points just upstream of the positive vortex cores at x/D = 5.5 & 9.6.

Profiles of phase-averaged streamwise intensity (random component) at Location V are plotted in Figure 18 when x_{usvl}/D = 5.5, 20.0, 30.0 & 40.0. These profiles have been made symmetric, $f_{sym}(y) = (f(y) + f(-y))/2$, because the final similarity analysis is for profiles that are obtained as an average of the effect of the passage of the upper and lower vortices and the accompanying braids. All the profiles have off-center peaks and a minimum at the wake centerline; thus, they resemble the time-averaged profiles of Fig. 15.

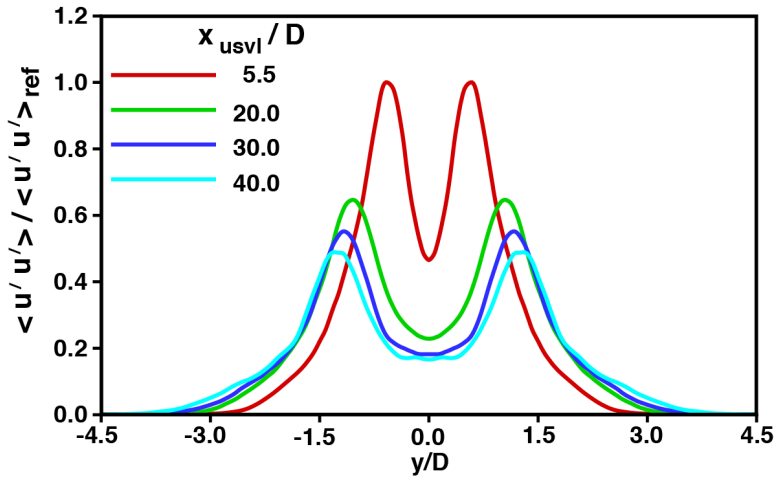

Figure 18. Profiles of streamwise intensity at Location V (random component) for x_{usvl}/D = 5.5, 20.0, 30.0 & 40.0.

Figure 19 shows phase-averaged streamwise intensity profiles (random component, symmetrized as in Fig. 18) at Location M for x_{usvl}/D = 5.5, 20.0, 30.0 & 40.0. There is a significant change in profile shape as x_{usvl}/D increases from 5.5 to 40.0. At x_{usvl}/D = 5.5 there is a single peak located at the wake centerline. The profiles corresponding to x_{usvl}/D = 30.0 and 40.0 possess off-center peaks as in Figs. 15 & 18. The one obtained at x_{usvl}/D = 20.0 is transitional and exhibits a flat top. Both these sets of curves (Figs. 18 & 19) contribute to the corresponding profiles of Fig. 15. This is because the profiles of Fig. 15 are obtained as an integral over all phases and the profiles of Figs.18 & 19 are the profiles obtained at two of those phases.

The profile corresponding to x_{usvl}/D = 5.5 in Fig. 19 is the most likely contributor to the lack of self-similarity in Fig. 15. As argued in Rai (2011) this profile is an indicator of an additional velocity and length scale. Figure 17 aids in understanding the source of multiple length and velocity scales. One set of length/velocity scales corresponds to vortex core related peaks and the other to braid related peaks. As the braids become weaker with increasing x their contribution to the profiles diminishes and self-similar profiles are obtained with a single velocity and length scale. The slight off-center peaks in Fig. 19 for x_{usvl}/D = 30.0 & 40.0 are core-related; this can be gleaned from Fig. 17b.

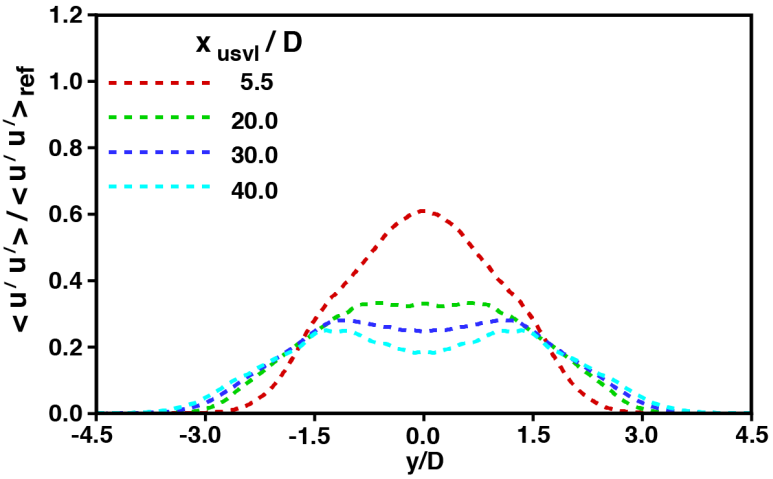

Figure 19. Profiles of streamwise intensity at Location M (random component) for x_{usvl}/D = 5.5, 20.0, 30.0 & 40.0.

Figure 20 shows profiles of the periodic component of phase-averaged streamwise intensity at Location V (symmetrized) for x_{usvl}/D = 5.5, 20.0, 30.0 & 40.0. These profiles also contribute to the profiles of Fig. 15. Except for the relatively low-magnitude intensity levels near the wake centerline all the profiles show off-center peaks as in Fig. 15 and are hence unlikely to contribute to a lack of profile self-similarity. Similar profiles (periodic component) at Location M were of low magnitude and not provided here.

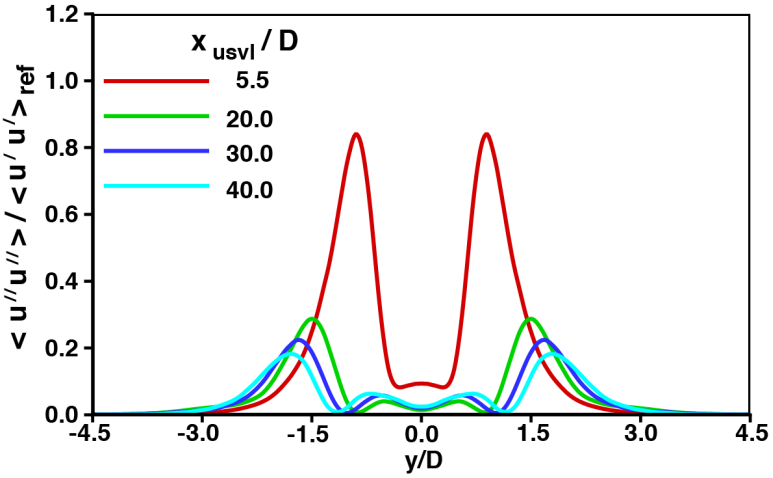

Figure 20. Profiles of streamwise intensity at Location V (periodic component) for x_{usvl}/D = 5.5, 20.0, 30.0 & 40.0.

In summary, the most likely contributor to the lack of profile similarity in the near wake is the braid related high streamwise intensity region. Its near disappearance with increasing x and the continued presence of core-related peaks results in self-similar profiles in the intermediate wake region.

As discussed earlier, in the cylinder case of **MA,** the time-averaged streamwise intensity profiles (periodic component) decrease rapidly with increasing x in relation to the total fluctuating value. The periodic profile is close to zero by x/D = 40.0; thus, the corresponding random component is the principal contributor to the total value. However, cross-stream intensity profiles show that the periodic component is the dominant contributor to the total value at x/D = 10.0 and makes a significant contribution to the total value

even at x/D = 40.0. Figure 21a shows the time-averaged random and periodic components of streamwise intensity at x/D = 5.5 & 40.0 for Case AX. Figure 21b shows the corresponding profiles for the cross-stream intensity. The trends of **MA** are observed here as well.

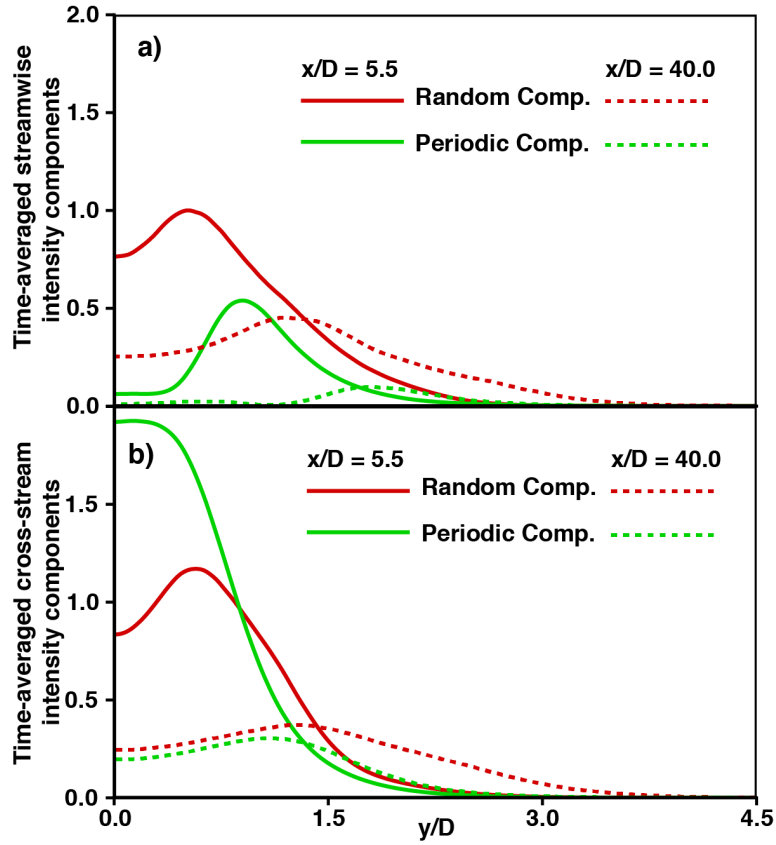

Figure 21. Profiles of time-averaged random & periodic components of a) streamwise and b) cross-stream intensity.

We conclude this first analysis of the intermediate wake of Case AX with a brief comparison of streamwise and cross-stream intensity distributions obtained in Case AX with those of a thin plate (Case F, Re_D = 625, Re_L = 1.25 x 10^6) from Rai (2017 & 2018b).

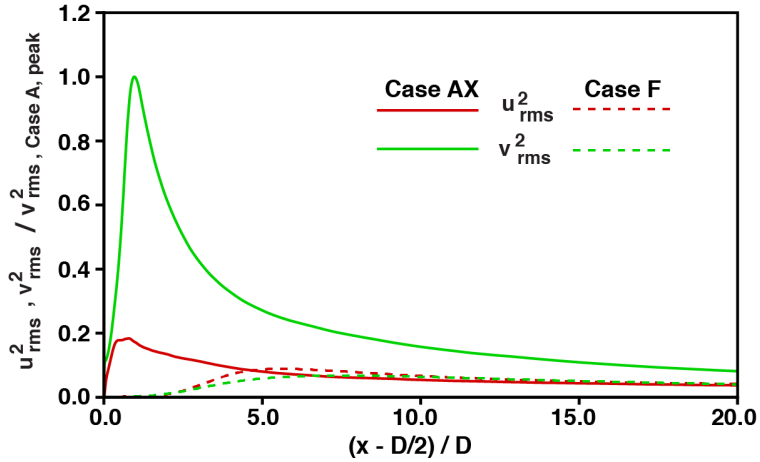

Figure 22. Variation of streamwise and cross-stream intensities (total value) along the wake centerline in Cases AX and F.

The shed vortices of Case F are much weaker than those of Case AX, are about 1.0D - 4.0D in spanwise length, and show considerable variation in both strength and frequency. Figure 22 shows the variation of the two components of intensity (total value) along the wake centerline for Cases AX and F. There is a substantial reduction in peak value of cross-stream intensity and the peak itself occurs further downstream (distance measured in terms of D) as we move from Case AX to Case F (increasing θ/D where θ is the TE momentum thickness). This is because the shed vortices are weaker and reach their peak strength further downstream as θ/D is increased. While the streamwise intensity level is also diminished with increasing θ/D, much of it is inherited from the boundary layer and therefore is not affected to the same extent. Another feature of interest is that while the peak in cross-stream intensity is higher than the peak in streamwise intensity in Case AX, the reverse is true in Case F. The primary cause for the reversal in trend is again the relative weakness of the shed vortices in Case F that results in significantly diminished cross-steam intensity levels.

5. CONCLUDING REMARKS

The intermediate wake region of a thick flat plate with a circular trailing edge is investigated with a direct numerical simulation. The upper and lower separating boundary layers are both turbulent. Earlier research dealt with the near/very-near wake of thick flat plates ($x/D < 13.0$). In the present investigation the emphasis is on the evolution of shed-vortex structure and turbulence intensity distributions for larger values of x/D. The focus is on the region $20.0 < x/D < 40.0$. Profile similarity in velocity statistics is explored.

Unlike the cylinder case, Case AX does not display the same level of shed-vortex distortion/rupture. In addition, the across-centerline movement of shed vortices that is prevalent past $x/D = 20.0$ in the cylinder case, is essentially absent in Case AX. The stability of the vortex street in Case AX has engineering implications (for example, unsteady loads on downstream rows of airfoils in turbomachinery caused by wakes generated in upstream airfoil rows).

Time-averaged velocity, turbulence intensity and shear stress distributions in the intermediate wake are considerably simpler than in the near wake. Velocity defect and time-averaged intensity profiles in the intermediate wake were found to be self-similar for the velocity and length and scales used here. Earlier research had shown that conventional scaling does not yield self-similarity of velocity and intensity profiles in the near wake because of the presence of more than one velocity and length scale. Multiple scales arise because the velocity and length scales associated with the braid region are different from those in the vortex core region. Because braid related intensity levels decay more rapidly than vortex-core related intensity levels with increasing x, there seems to be only one set of dominant scales remaining in the intermediate wake, thus resulting in the observed self-similarity in this region of the wake. This raises the question: Is the self-similarity in the intermediate wake maintained when the shed vortices ultimately break up? Obtaining an answer to this question via DNS will require a well resolved wake region that continues further downstream than the one used here (perhaps much further downstream).

REFERENCES

Cantwell, B. & Coles, D. 1983 An experimental study of entrainment and transport in the turbulent near wake of a circular cylinder. *J. Fluid Mech.* **136**, 321.

George, W. K. 1989 The Self Preservation of Turbulent Flows and its Relation to Initial Conditions and Coherent Structures. Advances in Turbulence, Eds. George, W. K. & Arndt, R., Hemisphere Publishing Corporation.

Hah, C., and Lakshminarayana, B. 1982 Measurement and Prediction of Mean Velocity and Turbulence Structure in the near Wake of an Airfoil. *J. Fluid Mech.*, **136**, 1982, 251.

Hussain, A.K.M.F. & Hayakawa, M. 1987 Eduction of large-scale organized structures in a turbulent plane wake. *J. Fluid Mech.* **180**, 193.

Hayakawa, M. & Hussain, F. 1989 Three-dimensionality of organized structures in a plane turbulent wake. *J. Fluid Mech.* **206**, 375.

Karlsson, R. I. & Johansson, T. G. 1988 LDV Measurements of higher-order moments of velocity fluctuations in a turbulent boundary layer. Laser Anemometry in Fluid Mechanics, Ladoan-Instituto Superior Tecnico, Portugal, 273.

Kim, J., Moin, P. & Moser, R. 1987 Turbulence Statistics in fully developed channel flow at low Reynolds number. *J. Fluid Mech.* **177**, 133.

Matsumura, M. & Antonia, R. A. 1993 Momentum and heat transport in the turbulent intermediate wake of a circular cylinder. *J. Fluid Mech.* **250**, 651.

Ong, L., Wallace, J., & Moin, P. 1995 The velocity and vorticity fields of the turbulent near wake of a circular cylinder. NASA TM -110513.

Rai, M. M. & Moin, P. 1991 Direct simulations of turbulent flow using finite-difference schemes. *J. Comp. Physics* **96** (1), 15.

Rai, M. M., 2008 Towards direct numerical simulations of turbulent wakes. Paper 2008-0544, 46th AIAA Aerospace Sciences Meeting, Reno, Nevada.

Rai, M. M. 2011 Flow physics and self-similarity in the turbulent near wake of a flat plate. Paper 2011-3575, 41st AIAA Fluid Dynamics Conference, Honolulu, Hawaii.

Rai, M. M. 2013 Flow physics in the turbulent near wake of a flat plate. *J. Fluid Mech.*, **724**, 704.

Rai, M. M. 2014 Flow Phenomena in the very near wake of a flat plate with a circular trailing edge. *J. Fluid Mech.*, **756**, 510.

Rai, M. M. 2015 Detached shear-layer instability and entrainment in the wake of a flat plate with turbulent separating boundary layers. *J. Fluid Mech.*, **774**, 5.

RAI, M. M. 2017 Changes in flat plate wake characteristics obtained with decreasing plate thickness. *International Journal of Heat and Fluid Flow*, **68**, 13.

Rai, M. M. 2018a Shed vortex structure and phase-averaged velocity statistics in symmetric/asymmetric turbulent flat plate wakes. *Physics of Fluids*, **30** (5), 055104_1-15.

RAI, M. M. 2018b Vortex Shedding Characteristics of the Wake of a Thin Flat Plate with a Circular Trailing edge. *International Journal of Heat and Fluid Flow*, **72**, 20.

Reynolds, W. C. & Hussain, A. K. M. F. 1972 The mechanics of an organized wave in turbulent shear flow. Part 3. Theoretical models and comparisons with experiments. *J. Fluid Mech***. 54**, 263.

Thomas, F. O., & Liu, X. 2004 An experimental investigation of symmetric and asymmetric turbulent wake development in pressure gradient. *Physics of Fluids*, **16**, (5), 1725.